

Flow dynamics and wall shear-stress variation in a fusiform aneurysm

Gregory J. Sheard

Received: 8 April 2008 / Accepted: 13 November 2008 / Published online: 4 December 2008
© Springer Science+Business Media B.V. 2008

Abstract Pulsatile flow through a tube featuring a sinusoidal bulge is computed in order to determine the flow dynamics and wall shear-stress conditions encountered under conditions representative of blood flow through a human abdominal aortic aneurysm. A high-order spectral-element algorithm is employed to accurately determine velocity and vorticity fields, plus wall shear stresses, which are notoriously difficult to measure experimentally. A greater level of detail in the flow is revealed when compared to recent particle image velocimetry experiments. For both the mean and standard deviation of wall shear stress, minimum levels are found at the widest point of the aneurysm bulge, and maximum levels are recorded in the distal (downstream) region of the bulge. In an aneurysm with length and maximum diameter 2.9 and 1.9 times the artery diameter, respectively, peak instantaneous wall shear stress is 2.4 times greater than the peak wall shear stress recorded in a healthy vessel.

Keywords Aneurysm · Blood flow · Computational fluid dynamics · Direct numerical simulation · Spectral-element method · Wall shear stress

Abbreviation

WSS Wall shear stress

1 Introduction

Aneurysms are a vascular disease, characterized by a local enlargement of an artery, that develop as the vessel-wall tissue weakens [1]. Factors that contribute to the weakening of the wall tissue include genetic predisposition [2],

G. J. Sheard (✉)
Division of Biological Engineering, Faculty of Engineering, Monash University, Clayton, VIC 3800, Australia
e-mail: Greg.Sheard@eng.monash.edu.au

G. J. Sheard
Fluids Laboratory for Aeronautical and Industrial Research (FLAIR), Department of Mechanical and Aerospace Engineering,
Monash University, Clayton, VIC 3800, Australia

lifestyle [3], and irregular wall shear stress [4]. As the wall tissue loses integrity, a positive feedback loop is initiated leading to further enlargement of the aneurysm. Ultimately, this can lead to rupture of the aneurysm. For aneurysms on major arteries such as the abdominal aorta, rupture is catastrophic [5], leading to death from internal bleeding in 75–90% of cases. The mortality rate is still almost 50% if rupture occurs at a medical facility [6]. Wall shear stress is a function of the fluid mechanics of blood, and therefore an understanding of the development of aneurysms requires an understanding of the blood-flow dynamics therein. This forms the basis of the present study.

Studies have identified that endothelial cells lining the interior of blood-vessel walls are susceptible to damage under excessive levels of wall shear stress [7], with a measured yield stress of 37.9 ± 8.5 Pa reported. This value is somewhat higher than the maximum wall shear stress measured in a healthy abdominal aorta (4.5 Pa [8]). Other studies [9] have demonstrated a correlation between reduced fluctuation in wall shear stress and thickening of the innermost layer of the vessel wall. Hence the integrity of the wall of an artery can suffer from atypical wall shear-stress environments featuring either excessive or inadequate stress levels.

Aneurysm geometries can be categorized as either fusiform or saccular. Fusiform aneurysms are the focus of the present study, and manifest as a widening about the vessel centreline, whereas saccular aneurysms emerge as a growth from one side of the vessel [1]. The most common location for aneurysms is the aorta [10], where they are also most dangerous. They can also form in other locations such as the head (cerebral aneurysm [11]), chest (thoracic aneurysm), and behind the kneecap (popliteal aneurysm [12]).

Medical research has explored the potential offered by numerical simulation to the study of aneurysm fluid mechanics and wall shear stresses (e.g. [10]). Typically these studies have considered only a single aneurysm geometry reconstructed from medical imagery, and hence fail to establish reliable parameter-dependence for the computed flows.

A recent experimental investigation attempted to systematically investigate aneurysm fluid dynamics through variation in geometric parameters [13]. In that study velocity fields within *in vitro* aneurysm models were measured using particle image velocimetry (PIV). However, limitations in resolution occluded structural detail in contour plots of flow within the models, and resulted in under-prediction of shear stresses in the flow (see [14] for a discussion of error in velocity gradient quantities derived from PIV measurements). In particular, over a pulse cycle, they found smaller peak wall shear stresses within the aneurysm than in a healthy vessel. A range of aneurysm geometries were studied at a Reynolds number and pulse frequency consistent with a human abdominal aortic aneurysm. The present study computes flow in a model aneurysm under conditions matching *Model 3* in that study.

The potential for numerical simulation of aneurysmal blood flow to contribute to our understanding of the fluid dynamics within aneurysms has been recognised [1]. Computational simulation of flow through tubes or vessels is not subject to the challenges inherent in accurately capturing the near-wall velocity field. Internal reflections add detectable “ghost particles” which contaminate the near-wall PIV correlations, eroding the measured near-wall velocities [15]. With appropriate grid refinement and boundary treatment, velocity, velocity gradient, and pressure fields can be determined accurately, particularly in the vicinity of vessel walls, where problems associated with refraction and total internal reflection are most pronounced.

The objective of this paper is to apply high-resolution numerical simulation to provide a detailed understanding of both the flow structures and dynamics within an aneurysm subjected to a realistic pulsatile flow, as well as the wall shear-stress variation and distribution through and in the vicinity of the aneurysm.

In this paper, Sect. 2 describes the problem under investigation, with Sect. 2.1 defining the aneurysm model. Sect. 2.2 presents the governing equations and describes the numerical discretisation of the problem. Section 2.3 details the establishment of a realistic pulsatile pulse waveform, and Sect. 2.4 outlines a particle tracking algorithm.

Section 3 presents the results of the study, which comprise sequences of contour plots of various flow quantities, and plots of the variation and statistical properties of wall shear stress throughout the model.

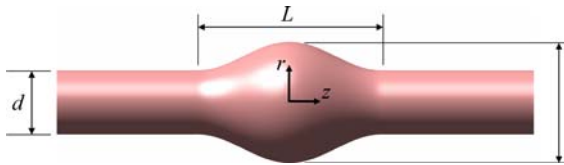


Fig. 1 Schematic diagram of geometry under investigation, showing key dimensions and the cylindrical ($z-r$) coordinates. Fluid flows through the interior of the model

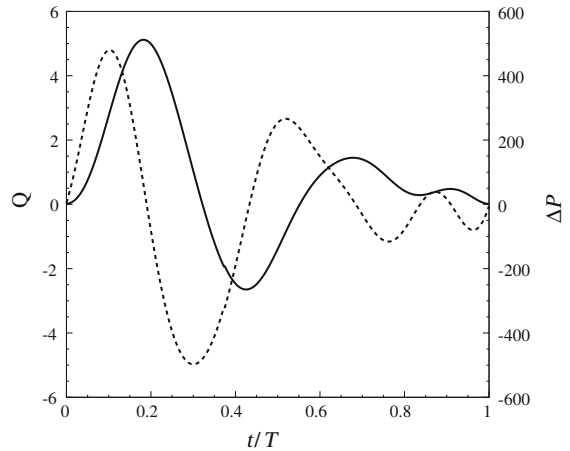


Fig. 2 Flow rate (Q , solid line) and the imposed pressure drop across the tube (ΔP , dotted line) plotted over a single period (T) for the case represented in Fig. 4

2 Problem formulation

2.1 Aneurysm model

The system under investigation in this paper comprises a circular tube of diameter d featuring an axisymmetric bulge, and fluid flows through the tube driven by a time-varying pressure gradient. The bulge is defined by a sinusoidal profile, with length L and maximum diameter D . Figure 1 illustrates this geometry. Relative to a cylindrical ($z-r$) coordinate system centered at the middle of the bulge, the tube wall and bulge are therefore defined by the function

$$r'(z') = \begin{cases} 1/2 & \text{if } |z'| > LR/2 \\ \frac{DR+1}{4} + \frac{DR-1}{4} \cos\left(\frac{2\pi z'}{LR}\right) & \text{if } |z'| \leq LR/2, \end{cases} \tag{1}$$

where primes denote non-dimensionalisation by d , and a diameter ratio $DR = D/d$ and length ratio $LR = L/d$ have been introduced.

2.2 Governing equations

The flow is assumed axisymmetric, following observations that blood flow in fusiform aneurysms is dominated by axisymmetric flow structures [1]. The axisymmetric governing equations in cylindrical coordinates are written

$$\begin{aligned} \frac{\partial u_z}{\partial t} + \left(u_z \frac{\partial u_z}{\partial z} + u_r \frac{\partial u_z}{\partial r} \right) &= -\frac{\partial P}{\partial z} + \nu \left[\frac{\partial^2 u_z}{\partial z^2} + \frac{1}{r} \frac{\partial}{\partial r} \left(r \frac{\partial u_z}{\partial r} \right) \right], \\ \frac{\partial u_r}{\partial t} + \left(u_z \frac{\partial u_r}{\partial z} + u_r \frac{\partial u_r}{\partial r} \right) &= -\frac{\partial P}{\partial r} + \nu \left[\frac{\partial^2 u_r}{\partial z^2} + \frac{1}{r} \frac{\partial}{\partial r} \left(r \frac{\partial u_r}{\partial r} \right) - \frac{u_r}{r^2} \right], \\ \frac{\partial u_z}{\partial z} + \frac{\partial u_r}{\partial r} + \frac{u_r}{r} &= 0, \end{aligned}$$

where the advection term is shown in convective form, t is time, ν is the kinematic viscosity, P is the kinematic static pressure (ratio of static pressure to density), and the axial and radial velocity components are given by u_z and u_r , respectively.

The flows in this study are computed by solving these equations using a spectral-element method for spatial discretization of the flow domain, and a third-order accurate backwards-multistep time-integration algorithm to evolve the flow. The present code has previously been used to solve pressure-driven flows in tubes in [16]. No turbulence model is employed—instead all flow scales are resolved on the spectral-element grid.

The spectral-element method employs polynomial basis functions within each element, providing control over the resolution of the simulations on a given mesh by varying the element polynomial degree (p -refinement). The method also employs efficient Gauss–Legendre–Lobatto quadrature to solve the integral equations arising from the implementation of the spectral-element method, often resulting in spectral convergence characteristics with increasing element polynomial degree [17].

On the axis, a stress-free boundary is naturally imposed through the formulation of the solver in cylindrical coordinates [18]. Along the tube wall, a no-slip condition is imposed on the velocity field, and an appropriate high-order condition is imposed on the pressure gradient [17]. The imposition of an appropriate Neumann boundary condition for pressure preserves the third-order temporal accuracy of the scheme. The flow is driven by a pressure gradient (ΔP) imposed by enforcing a zero reference pressure at the downstream boundary, and a time-varying pressure at the upstream boundary.

A Newtonian fluid viscosity model is employed, describing a linear relationship between shear stress and strain. This replicates the conditions of the experiments conducted in [13]. While the concentrated suspension of blood cells can yield non-Newtonian behaviour, blood is found to behave largely as a Newtonian fluid in larger vessels [19] such as the aorta, which motivates this study. Furthermore, in [20] the non-Newtonian properties of arterial blood flow was considered, with variation from Newtonian flow being isolated to the centreline of arteries, away from the walls, where the interest of the present study is focused.

Dynamic similarity of pulsatile Newtonian flow is achieved by matching two dimensionless parameters, the Reynolds number and Womersley number.

The Reynolds number relates inertial to viscous effects in a flow, and is defined

$$\text{Re} = \frac{Ud}{\nu}, \quad (2)$$

where U is the time-averaged velocity in the tube, given by $U = \bar{Q}/A$. Here \bar{Q} is the time-average volume flow rate and A is the tube cross-section area $\pi d^2/4$.

The Womersley number characterises the frequency of a pulsatile flow, and is defined

$$\alpha = \frac{d}{2} \sqrt{\frac{2\pi f}{\nu}}, \quad (3)$$

where f is the frequency of the pulsatile waveform.

In a fluid flow, the local rate of rotation is obtained from the curl of the velocity field (the vorticity, ω). Vorticity is Galilean-invariant, meaning that its value is independent of the coordinate system used. When combined with the observation that, along a wall, the no-slip condition provides zero tangential velocity gradients, the Galilean-invariance of vorticity can be used to show that wall shear stress is related to the vorticity at the wall by

$$\text{WSS} = \mu\omega|_{\text{wall}}, \quad (4)$$

where μ is the dynamic viscosity. Dimensionless vorticity and wall shear-stress values reported in this study can be converted to dimensional values by multiplying by U/d and $\mu U/d$, respectively. Hereafter, all quantities are expressed in dimensionless form, with the primes omitted for clarity. Time is normalised by d/U , velocities by U , and spatial coordinates by d .

Flow conditions $\text{Re} = 330$ and $\alpha = 10.7$ were employed in [13] to model conditions within a human abdominal aorta. The same Reynolds number and Womersley number are used throughout this study, and an aneurysm with dimensions $\text{LR} = 2.9$ and $\text{DR} = 1.9$ is considered, corresponding to *Model 3* in that study.

2.3 Pulsatile blood flow

In 1955, Womersley [21] published an analytical solution for the time-varying velocity profile and flow rate in a straight circular tube subject to a periodic pressure gradient. In that paper, the complex Fourier coefficients of the pressure gradient were related to the Fourier coefficients of the corresponding flow rate. From that study, a relationship between the dimensionless Fourier coefficients of the present imposed kinematic static pressure drop (ΔP_k) and the mean velocity (\bar{u}_k), given as

$$\Delta P_0 = -\frac{32L_{\text{tot}}}{\text{Re}} \bar{u}_0, \quad \Delta P_k = \frac{i \frac{4L_{\text{tot}}}{\text{Re}} \alpha_k^2 \bar{u}_k}{1 - \frac{2}{\alpha_k i^{3/2}} J_1(\alpha_k i^{3/2}) / J_0(\alpha_k i^{3/2})}, \quad (5)$$

where Bessel functions of the zeroth (J_0) and first (J_1) order with complex arguments are employed, L_{tot} is the dimensionless length of the computational domain (here $L_{\text{tot}} = 32.9$), and $\alpha_k = \sqrt{k} \alpha$ characterises the frequency of the k th mode. The appearance in these expressions of the imaginary number i implies that the pressure drop and flow rate are out of phase, and the expression shows that the phase angle is in fact a non-trivial function of α . In other words, the phase difference between pressure drop and flow rate varies with the frequency of the waveform components.

To produce a tube flow rate waveform consistent with that used in [13], an aortic blood flow waveform measured in [22] was digitized and decomposed into complex Fourier series coefficients. Equation (1) was used to determine the corresponding coefficients of the pressure drop.

Strictly, Eq. 1 only applies to the Fourier coefficients for flow in a straight circular tube. However, as the aneurysm bulge only occupies a small portion of the otherwise uniform tube computed in this study, the relationship still provides pressure drop coefficients that produce a time-varying flow consistent with the experiments of [13] and measurements of [22]. Figure 2 plots both the imposed pressure-drop waveform and computed flow rate for an aneurysm model with LR = 2.9 and DR = 1.9, at Re = 330 and $\alpha = 10.7$. Notice the substantial phase lag between the waveforms of pressure-drop and flow rate.

Due to the perturbed flow in the aneurysm bulge, a nonlinear relationship existed between the kinematic viscosity (available as a control parameter in the computations), and the Reynolds number (derived from the time-average of the resulting periodic flow rate through the tube). Subjected to the imposed pressure drop (Fig. 2), the flow converged to a periodic state with the target Reynolds number Re = 330 when $1/\nu = 316.85/Ud$.

2.4 Particle tracking

A simulated particle tracking algorithm is employed to facilitate visualization of the flows analogous to dye-visualization employed regularly in experiment. The positions of simulated particles are evolved on the computational domain by means of a nearly fourth-order accurate time integration technique developed by [23]. Within elements, particle positions are advanced using a fourth-order Runge–Kutta method in parametric space, and a series of first-order sub-steps are taken to advance to, and cross, element interfaces. Sheard et al. [24] proposed a visualization method plotting particle concentration, which is calculated by summing the number of particles in the vicinity of each data point limited by a Gaussian mask. The variance of the Gaussian mask is varied with mesh density to minimize Moiré artifacts.

2.5 Grid independence

The pulsatile pressure waveform driving the flow permits reversed flow during each pulse cycle. This has serious implications on the numerical stability of the scheme should traditional outflow boundary conditions be employed. To avoid this, a periodic condition is imposed, linking the velocity field leaving the outlet to that entering the inlet. To isolate the effect of a single aneurysm bulge, a sufficient length of straight tube was included in the computational

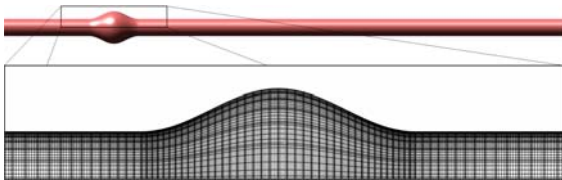


Fig. 3 Top: The full computational domain. Inset: Detail of the mesh in the vicinity of the aneurysm bulge. Interpolation points corresponding to 7th-degree polynomials within each element are shown

Fig. 5 A plot of flow rate against time over one period, at $Re = 330$ and $\alpha = 10.7$, with $DR = 1.9$ and $LR = 2.9$. Symbols indicate the times at which the frames in Figs. 6–7 were obtained

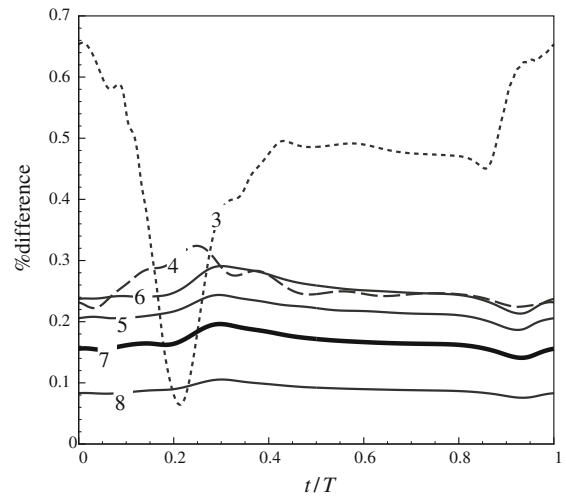
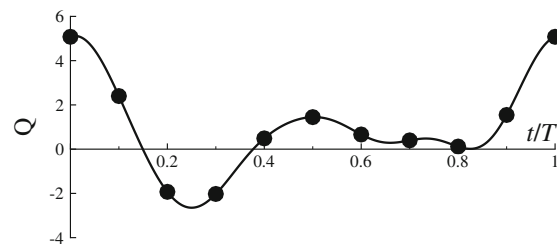


Fig. 4 Percentage differences in flow rate over a single pulse period of various element polynomial degrees (labeled) compared to a simulation with polynomial degree 9. The flows were computed at $Re = 330$ and $\alpha = 10.7$, for a model with $DR = 1.9$ and $LR = 2.9$. The element polynomial degree used in this paper, 7, is shown in *bold*



domain to allow vortical structures generated within the bulge to dissipate before returning to the aneurysm bulge. The computational domain and spectral-element mesh is shown in Fig. 3.

A p -refinement study was conducted to find a suitable element polynomial degree which was sufficient to accurately resolve the flow over the parameter range of this study. A model with $LR = 2.9$ and $DR = 1.9$ was computed at $Re = 330$ and $\alpha = 10.7$ for polynomial degrees ranging from 3 to 9. Once periodic flow was achieved in each simulation, percentage differences in the flow rate over a single period were calculated for each polynomial degree compared to the highest-resolution case. Trends of these differences are plotted in Fig. 4. The trends achieved with polynomial degrees 3 and 4 are inconsistent with those of higher resolution, indicating that these resolutions were insufficient to resolve the flow adequately. For the remainder of this study, elements with polynomial degree 7 are used, which provide discrepancies of less than 0.2% in computed flow rate.

3 Results

Computations were performed on a model with $LR = 2.9$ and $DR = 1.9$, at $Re = 330$ and $\alpha = 10.7$. Simulations were evolved to a periodic state, and data was acquired at a set of discrete intervals over a complete pulse cycle. Figure 5 shows the locations of these sample points in relation to the measured flow rate waveform.

In experiment, the transport of a visualization medium (e.g. fluorescent dye; see [25,26]) has been used widely to determine the topology of a fluid flow. Here a stream of simulated particles was injected into the flow upstream of the aneurysm near the tube wall, and a sequence of images showing the kinematic transport of this particle stream over a full pulse period is shown in Fig. 6. Frame (a) shows the flow at peak systole (peak forward flow). As the flow rate begins to decrease (frame (b)), particles can be seen rolling up into a vortex located just downstream of the middle of the aneurysm. This vortex enlarges through frame (c), and in frame (d) its anti-clockwise rotation couples with reversed flow in the tube to generate a weaker vortex of opposite rotational direction located near the proximal (upstream) end of the bulge. This secondary vortex is not clearly identified by particles in subsequent frames, but

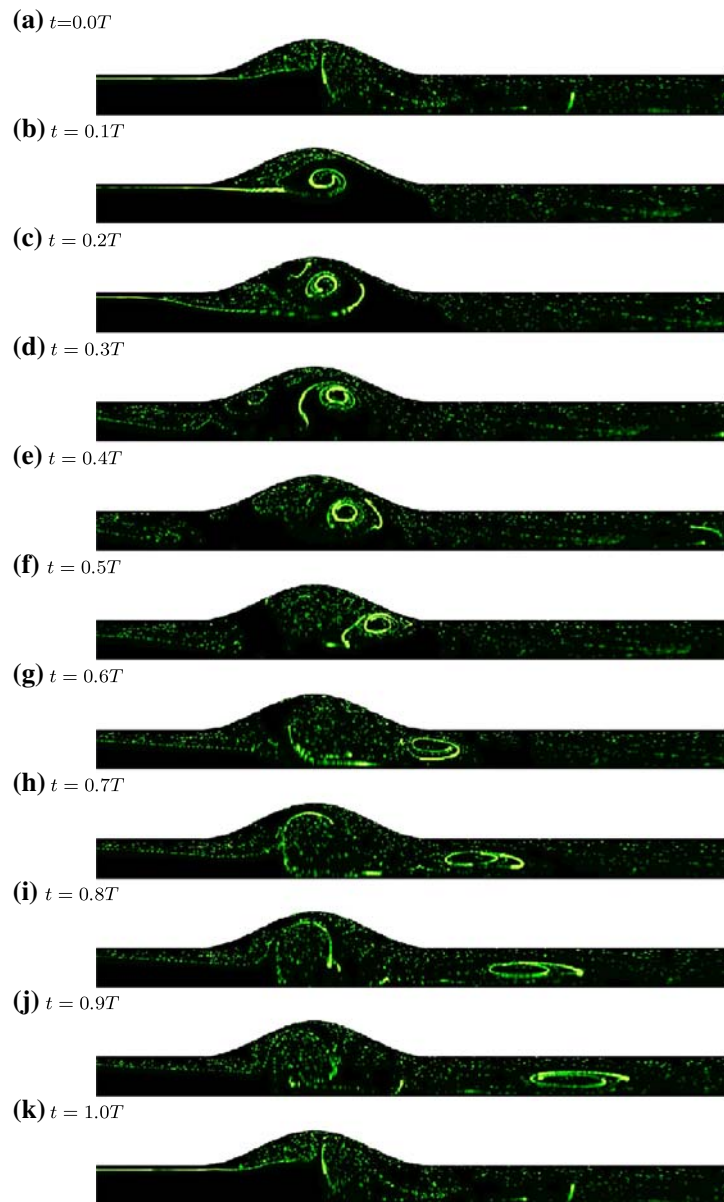


Fig. 6 The transport of simulated particles injected upstream of the bulge. Flow is left to right, the meridional half-plane is plotted, and the computation was conducted at $Re = 330$, $\alpha = 10.7$, $DR = 1.9$ and $LR = 2.9$. 10 snapshots are taken over one period of the flow. Bright regions show high particle concentration [24]

the original vortex can be seen migrating out of the aneurysm bulge and downstream through frames (e–j). Frame (k) marks the end of the cycle and return to peak systole, and by this time the vortex has convected out of the field of view to the right.

It is sometimes dangerous to equate structures visible in dye or simulated particles with vortical structures in a flow (highlighted recently in [24]). While Fig. 6 facilitates comparison with visualization in experiments, the vortical dynamics of the flow are more clearly displayed by plots of vorticity. Figure 7 plots contours of vorticity over the same sequence.

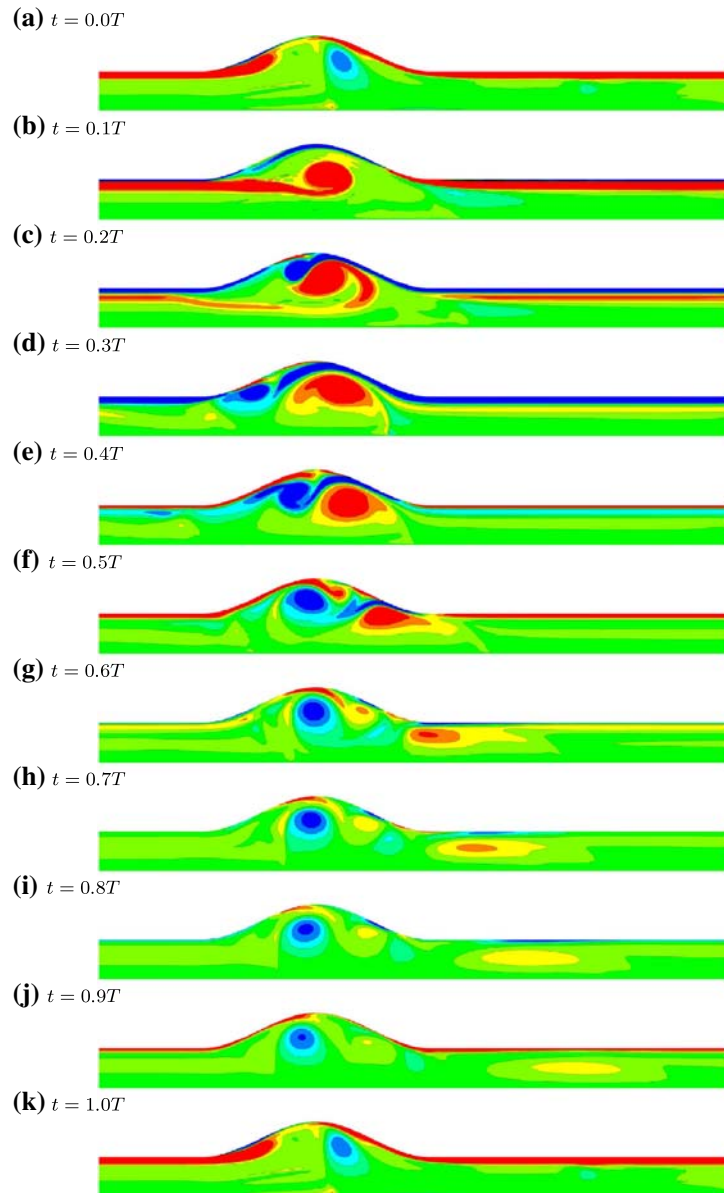


Fig. 7 Dimensionless out-of-plane vorticity contours plotted for the same frames shown in Fig. 6. Eight equi-spaced contour levels are plotted between -20 (blue) and 20 (red)

A similar sequence of vorticity plots generated from PIV measurements is provided in [13]. The resolution limitations of that study are apparent in that contours of vorticity at the model walls are confined to within a single grid spacing. Figure 7b here shows the strong vortex ring shed from the proximal end of the aneurysm bulge which was also detected in the earlier experiments. However, in later frames, flow structures in the PIV measurements reduce in strength and are difficult to distinguish from background noise. Figure 7 reveals that the flow at subsequent times through the pulse cycle features the generation of an opposite-sign vortex ring which persists in the bulge, while the original vortex ring is ejected out of the bulge and into the distal vessel. The opposite-sign vortex ring would naturally propagate in the upstream direction owing to the induced velocity of the vortex core on the opposite side of the ring. This may explain why this secondary vortex ring remains upstream of the centre of the bulge from frames (c) to (j). In contrast, the primary vortex ring naturally self-propels downstream, quickly distancing itself from secondary vortex structure. These computational simulations have revealed the true complexity of this flow, and the variation in strength and sign of the vorticity near the wall demonstrates the complexity of the wall shear stresses induced by pulsatile flow within an aneurysm. In particular, the vorticity contour plots reveal regions of high shear along the straight tube walls (frames (a) and (c)), as well as local regions of high shear at intermittent times and locations within the aneurysm bulge.

Dimensionless wall shear stress was sampled at a number of points on the tube wall upstream, downstream and throughout the aneurysm bulge. These measurements are plotted in Fig. 8 at times corresponding to the sequences of frames shown in Figs. 6–7.

Figure 8 demonstrates subtle features of the variation in wall shear stress over time and as a function of position along the tube wall. In frame (a), corresponding to peak systole, a peak in the shear stress is observed in the distal end of the aneurysm ($0 \lesssim z \lesssim 1.45$). This peak has a value 2.4 times greater than the level recorded in the straight portions of the tube at that time. Over subsequent frames (b–e), the peak stress gradually diminishes, though in these frames it remains significantly larger in value than the peak value recorded in the healthy sections of the tube (occurring in frame (a)). Later frames (in particular frames (g–i)) exhibit smaller stresses, sometimes almost zero throughout the tube and aneurysm. These times correspond to the resting period of the pulse cycle.

To determine how the wall shear stress measured in the aneurysm bulge differs from the levels and variation of wall shear stress in healthy vessels, time mean and standard deviations were measured over a pulse cycle at each sample location plotted in Fig. 8. The resulting plots are shown in Fig. 9. It is interesting to note that significant deviation from the values obtained in the straight tube sections are isolated to the aneurysm bulge ($|z| \lesssim 1.45$). Figure 9a shows that within this aneurysm model, the minimum and maximum mean values of the magnitude of the wall shear stress are 38% and 173% of the values found in the un-dilated tube sections, respectively. However, when considering the time mean of the wall shear stress itself, a peak is found 4.0 times greater than the mean level in the healthy vessel, and an opposite-sign peak is found with a level 7.3 times greater than the healthy level. These elevated levels of wall shear stress may lead to damage of the endothelium on the distal aneurysm wall [7].

The standard deviation trends in Fig. 9b show that from the proximal end of the aneurysm to the mid-point, the standard deviation levels decrease, with minimum standard deviations being found at the mid-point of the aneurysm. These minima were 44–47% of the values obtained in a healthy vessel, possibly degrading the integrity of the intimal layer of the vessel wall [9]. Peaks in the standard deviation were found in the distal region of the aneurysm bulge. These peaks were 194% and 163% of the values found in a healthy vessel for WSS and $|WSS|$, respectively. The experiments of [13] determined wall shear-stress levels within their aneurysm models to be approximately 80% of those found in healthy vessels, while conceding that those values were being under-predicted because of a lack of resolution. Here wall shear-stress statistics demonstrate that in fact wall shear-stress levels (both in terms of a time-averaged level as well as the amount of fluctuation experienced at a given point) can differ significantly from the levels found in a healthy vessel. This likely contributes to a degradation of the health and mechanical durability of the vessel wall surrounding an aneurysm.

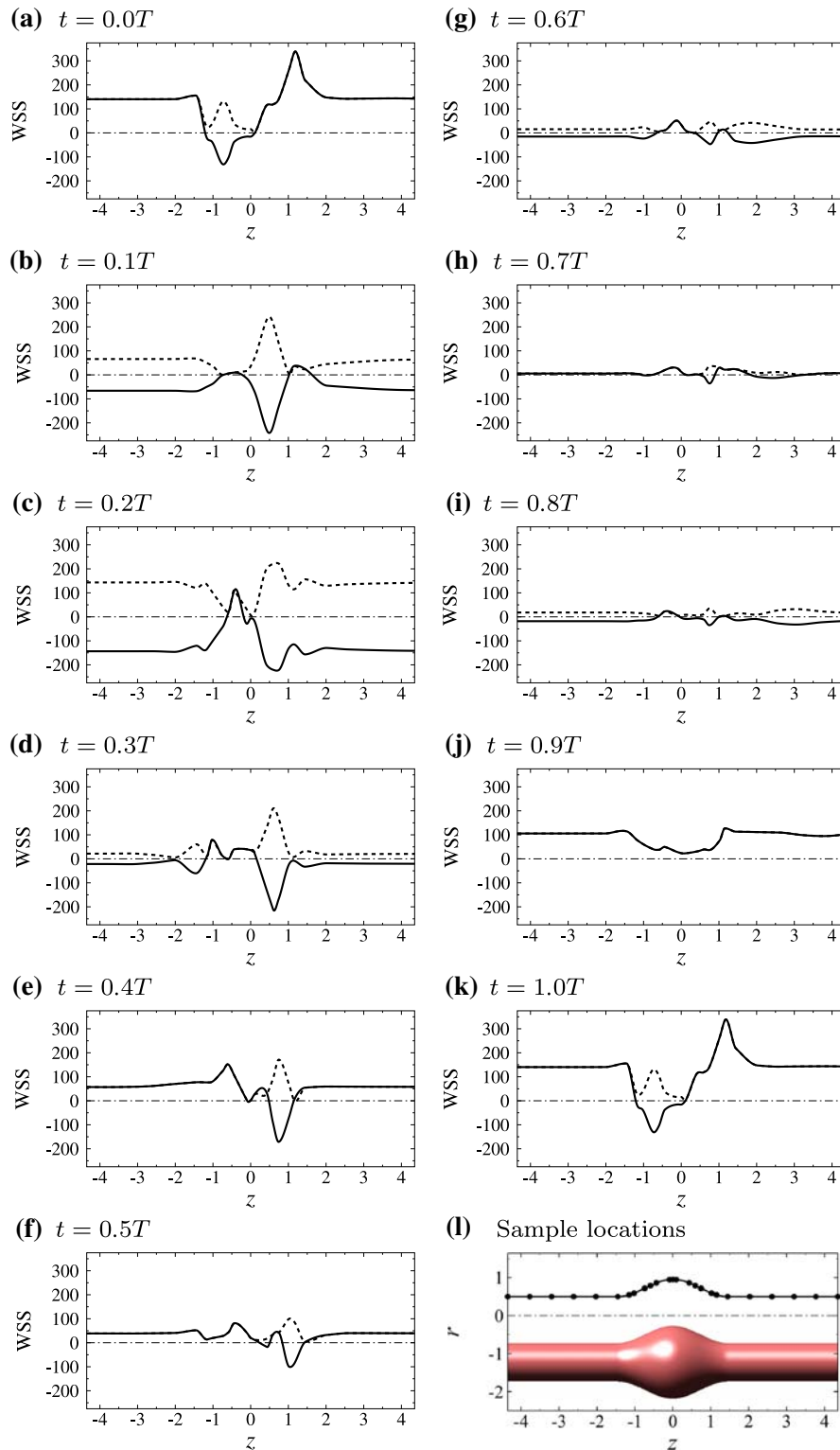
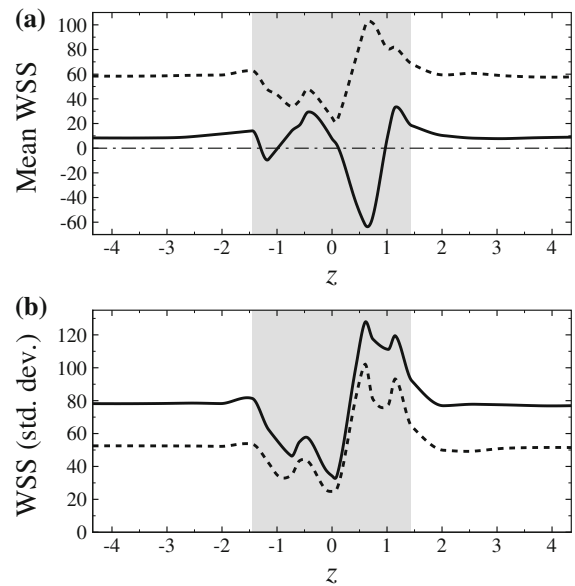


Fig. 8 Plots of dimensionless wall shear stress (*solid lines*) and its magnitude (*dotted lines*) at locations along the wall upstream, within, and downstream of the aneurysm bulge. Data was acquired from the solutions shown in Fig. 6

Fig. 9 Plots of (a) the local time mean of both the dimensionless wall shear stress (WSS; *solid line*) and its magnitude ($|WSS|$; *dotted line*), and (b) their standard deviations against axial position as per Fig. 5. Again, data was acquired at the conditions shown in Fig. 6. The *shaded region* corresponds to the location of the aneurysm bulge



4 Conclusions

Pulsatile flow has been computed in a model aneurysm defined by a sinusoidal bulge on a straight circular tube. The aneurysm dimensions ($LR = 2.9$, $DR = 1.9$) and flow parameters ($Re = 330$, $\alpha = 10.7$) correspond to a medium-sized aneurysm, typically considered low-risk, on a human abdominal aorta. The high-order spectral-element solver employed in this study has produced plots of vorticity within the aneurysm which achieve a greater level of detail and resolution than has been achieved using experimental imaging techniques to date. A secondary opposite-sign vortex ring structure has been revealed, in addition to the primary vortex ring known to develop from the proximal end of the bulge during the systolic phase. Wall shear-stress measurements have been conducted through the tube and aneurysm bulge, resulting in a detailed quantitative understanding of wall shear-stress variation within an aneurysm when compared to an un-dilated tube. Significantly higher mean and standard deviation in shear stress were recorded in the distal end of the aneurysm bulge, as compared to those values recorded in straight sections of the tube. Despite previous studies reporting smaller wall shear stresses within an aneurysm bulge subject to pulsatile flow, these computations reveal that under these conditions the highest wall shear stress is 2.4 times greater than the highest wall shear stress recorded in a healthy vessel. This peak value occurred at peak systole at the distal end of the aneurysm, whereas the widest point exhibited consistently the lowest levels of wall shear stress. In vivo experiments [27] have indicated that high levels of wall shear-stress encourages endothelial and smooth muscle cell development in aneurysms, which may enhance the integrity of the wall tissue. In contrast, low-flow (low wall shear stress) aneurysms exhibited significantly more growth, suggesting that the wall tissue in the centre of the bulge is most susceptible to aneurysm disease progression.

Acknowledgements This work was supported by the Monash Research for an Ageing Society (MonRAS) Research Support Scheme. Computations were performed using the Australian Partnership for Advanced Computing (APAC) National Facility, thanks to a time allocation under the Merit Allocation Scheme.

References

1. Lasheras JC (2007) The biomechanics of arterial aneurysms. *Ann Rev Fluid Mech* 39:293–319
2. Astradsson A, Astrup J (2001) An intracranial aneurysm in one identical twin, but no aneurysm in the other. *Br J Neurosurg* 15(2):168–171

3. Wilmink TBM, Quick CRG, Day NE (1999) The association between cigarette smoking and abdominal aortic aneurysms. *J Vasc Surg* 30:1099–1105
4. Kondo S, Hashimoto N, Kikuchi H, Hazama F, Nagata I, Kataoka H (1997) Cerebral aneurysms arising at nonbranching sites. An experimental study. *Stroke* 28(2):398–403
5. Rutherford RB (2006) Randomized EVAR trials and advent of level I evidence: a paradigm shift in management of large abdominal aortic aneurysms?. *Semin Vasc Surg* 19(2):69–74
6. Brown MJ, Sutton AJ, Bell PR, Sayers RD (2002) A meta-analysis of 50 years of ruptured abdominal aortic aneurysm repair. *Br J Surg* 89:714–730
7. Fry DL (1968) Acute vascular endothelial changes associated with increased blood velocity gradients. *Circ Res* 22:165–197
8. Oyre S, Pedersen EM, Ringgaard S, Boesiger P, Paaske WP (1997) In vivo wall shear stress measured by magnetic resonance velocity mapping in the normal human abdominal aorta. *Eur J Vasc Endovasc Surg* 13(3):263–271
9. Ku DN, Giddens DP, Zarins CK, Glagov S (1985) Pulsatile flow and atherosclerosis in the human carotid bifurcation. Positive correlation between plaque location and low oscillating shear stress. *Arterioscler Thromb Vasc Biol* 5:293–302
10. Raghavan ML, Vorp DA, Federle MP, Makaroun MS, Webster MW (2000) Wall stress distribution on three-dimensionally reconstructed models of human abdominal aortic aneurysm. *J Vasc Surg* 31(4):760–769
11. Kataoka K, Taneda M, Asai T, Kinoshita A, Ito M, Kuroda R (1999) Structural fragility and inflammatory response of ruptured cerebral aneurysms. A comparative study between ruptured and unruptured cerebral aneurysms. *Stroke* 30(7):1396–1401
12. Bouhouts J, Martin P (1974) Popliteal aneurysm—review of 116 cases. *Br J Surg* 61(6):469–475
13. Salsac A-V, Sparks SR, Chomaz J-M, Lasheras JC (2006) Evolution of the wall shear stresses during the progressive enlargement of symmetric abdominal aortic aneurysm. *J Fluid Mech* 560:19–51
14. Fouras A, Soria J (1998) Accuracy of out-of-plane vorticity measurements derived from in-plane velocity field data. *Exp Fluids* 25:409–430
15. Stanislas M, Okamoto K, Kähler C (2003) Main results of the first international PIV challenge. *Meas Sci Technol* 14:63–89
16. Sheard GJ, Ryan K (2007) Pressure-driven flow past spheres moving in a circular tube. *J Fluid Mech* 592:233–262
17. Karniadakis GE, Israeli M, Orszag SA (1991) High-order splitting methods for the incompressible Navier–Stokes equations. *J Comp Phys* 97:414–443
18. Blackburn HM, Sherwin SJ (2004) Formulation of a Galerkin spectral element—Fourier method for three-dimensional incompressible flow in cylindrical geometries. *J Comput Phys* 197:759–778
19. Wootton DM, Ku DN (1999) Fluid mechanics of vascular systems, diseases, and thrombosis. *Ann Rev Eng* 1:299–329
20. Rodkiewicz CM, Sinha P, Kennedy JS (1990) On the application of a constitutive equation for whole blood. *J Biomech Eng* 112:198–206
21. Womersley JR (1955) Method for the calculation of velocity, rate of flow and viscous drag in arteries when the pressure gradient is known. *J Physiol* 127:553–563
22. Maier SE, Meier D, Boesinger P, Moser UT, Vieli A (1989) Human abdominal aorta: comparative measurements of blood flow with MR imaging and multigated doppler US. *Radiology* 171(2):487–492
23. Coppola G, Sherwin SJ, Peiró J (2001) Non-linear particle tracking for high-order elements. *J Comp Phys* 172:356–386
24. Sheard GJ, Leweke T, Thompson MC, Hourigan K (2007) Flow around an impulsively arrested circular cylinder. *Phys Fluids* 19(8):083601
25. Williamson CHK (1996) Three-dimensional wake transition. *J Fluid Mech* 328:345–407
26. Sheard GJ, Thompson MC, Hourigan K, Leweke T (2005) The evolution of a subharmonic mode in a vortex street. *J Fluid Mech* 534:23–38
27. Hoshina K, Sho E, Sho M, Nakahashi TK, Dalman RL (2003) Wall shear stress and strain modulate experimental aneurysm cellularity. *J Vasc Surg* 37(5):1067–1074